Universal Optical Control of Chiral Superconductors and Majorana Modes

M. Claassen,[1] D. M. Kennes,[2] M. Zingl,[1] M. A. Sentef,[3] and A. Rubio[1,3]

[1]*Center for Computational Quantum Physics, Simons Foundation Flatiron Institute, New York, NY 10010 USA*

[2]*Dahlem Center for Complex Quantum Systems and Fachbereich Physik, Freie Universität Berlin, 14195 Berlin, Germany*

[3]*Max Planck Institute for the Structure and Dynamics of Matter, Center for Free Electron Laser Science, 22761 Hamburg, Germany*

(Dated: October 16, 2018)

Abstract

Chiral superconductors are a novel class of unconventional superconductors that host topologically protected chiral Majorana fermions at interfaces and domain walls [1–3], with great potential for topological quantum computing [4] and dissipationless electronic transport. Here we show that the out-of-equilibrium superconducting state in such materials is itself described by a Bloch vector in analogy to a qubit, which can be controlled all-optically on ultrafast time scales [5]. The control mechanism is universal and permits a dynamical change of handedness of the condensate. It relies on transient dynamical breaking of lattice rotation, mirror or time-reversal symmetries via choice of pump pulse polarization to enable arbitrary rotations of the Bloch vector. The underlying physics can be intuitively understood in terms of transient Floquet dynamics, however, the mechanism extends to ultrafast time scales, and importantly the engineered state persists after the pump is switched off. We demonstrate that these novel phenomena should appear in graphene [6–8] and magic-angle twisted bilayer graphene (TBG) [9–13], as well as Sr_2RuO_4 [14, 15], as candidate chiral $d + id$ and $p + ip$ superconductors, respectively, and show that chiral superconductivity can be detected in time-resolved pump-probe measurements. This paves the way towards a robust mechanism for ultrafast control and measurement of chirally-ordered phases and Majorana modes.

The search for Majorana fermions in condensed matter has recently generated much excitement [16–18], in particular due to their potential use in topological quantum computing [4]. A particularly intriguing realization can be found in quasi-two-dimensional chiral superconductors [3], for which the phase of the order parameter $\Delta(\mathbf{k})$ winds in either clockwise or counter-clockwise fashion about the Fermi surface, thereby spontaneously breaking time-reversal symmetry (TRS). Imbued with a non-trivial $\mathbb{Z}$ bulk topology [2], such materials host topologically-protected chiral Majorana modes at their boundaries [19] as well as vortices with non-Abelian statistics [20], constituting a superconducting analogy of the quantum anomalous Hall effect.

Over the past years, experimental evidence for the requisite TRS breaking and spin-triplet pairing has accumulated for Sr_2RuO_4 [14, 15]and UPt_3 [21, 22], rendering these materials candidate chiral $p+ip$ or $f+if$ superconductors. Moreover the recent discovery of superconductivity in magic-angle twisted bilayer graphene (TBG) [9] has spurred proposals of exotic $d_{x^2-y^2}+id_{xy}$ singlet pairing [12, 13], analogous to predictions for heavily-doped graphene monolayers [6–8]. However, a central follow-up question is how chiral condensates and associated Majorana modes can be probed and controlled.

Here we show that optical pumping permits universal control of the order parameter and handedness of chiral superconductors, and can serve as direct evidence of their chiral nature in time-resolved pump-probe experiments via tracking transient signatures of the nonequilibrium electronic order [23–25]. Central to the robustness of our predictions, the underlying effect works on ultrafast time scales, persists after the pump is off, and relies solely on symmetry arguments, hence making it applicable to any material described by a chiral order parameter. An immediate consequence is the possibility to optically define domains with a particular handedness of the chiral order parameter with chiral Majorana modes at their boundaries, depicted schematically in Fig. 1(a).

In unconventional superconductors, TRS can be spontaneously broken if the nodal pairing function is degenerate due to crystal symmetry [26]. The simplest manifestation of this is triplet p-wave pairing in a tetragonal crystal, where p_x and p_y nodal gap functions span a two-dimensional irreducible representation (irrep) E_u. The degeneracy derives from joint C_4 rotation and σ_v, σ_d mirror symmetries. Below the superconducting critical temperature T_C it is energetically favorable to spontaneously break TRS and parity in order to gap out the Bogoliubov band structure across the entire Fermi surface by forming a p_x+ip_y condensate.

As the choice of handedness is arbitrary, such a chiral pairing function is degenerate with its time-reversed Kramers partner $p_x - ip_y$. Similarly, in hexagonal D_6 or D_3 systems such as graphene or magic-angle TBG with C_6 or C_3 rotation and in-plane mirror or out-of-plane two-fold rotation symmetries, $d_{x^2-y^2}$, d_{xy} span the E_2 or E two-dimensional irrep, such that a chiral $d_{x^2-y^2} + id_{xy}$ state becomes energetically favorable.

The principal observation that constitutes the starting point for this work is that a chiral order parameter pushed out of equilibrium will cease to be constrained to the equilibrium free-energy minima $p + ip$ or $p - ip$ ($d + id$ or $d - id$), and instead evolve within the full two-dimensional subspace spanned by the corresponding irrep. Generically, a spatially homogeneous superconducting gap function within a two-dimensional irrep can be written as $\mathbf{\Delta}(\mathbf{k}) = \Delta \left[\cos\left(\frac{\theta}{2}\right) \hat{\boldsymbol{\eta}}^{(1)}_{\mathbf{k}} + e^{i\phi} \sin\left(\frac{\theta}{2}\right) \hat{\boldsymbol{\eta}}^{(2)}_{\mathbf{k}}\right]$. Here, Δ is the gap amplitude and $\hat{\boldsymbol{\eta}}^{(1,2)}_{\mathbf{k}}$ are explicit forms of the relevant two-dimensional irrep, for instance a chiral representation $\eta^{(1,2)}_{\mathbf{k}} = \sin(k_x) \pm i \sin(k_y)$ for nearest-neighbor p-wave pairing on the square lattice. One immediately sees that the out-of-equilibrium order parameter can be represented via a Bloch vector in direct analogy to a qubit [Fig. 1(b)], with $\mathbf{u} = [\sin(\theta)\cos(\phi),\ \sin(\theta)\sin(\phi),\ \cos(\theta)]^\top$.

We choose $\mathbf{u} = [0,\ 0,\ \pm 1]^\top$ to denote chiral $p_x \pm ip_y$ or $d_{x^2-y^2} \pm id_{xy}$ pairing, with nodal order parameters lying on the Bloch sphere equator.

An optical pulse can now selectively reduce the symmetry group via choice of the light polarization and induce controlled dynamics of the Bloch vector. A linearly-polarized laser pulse necessarily breaks C_3, C_4 or C_6 discrete lattice rotation symmetries, while preserving mirror symmetries if the polarization vector is collinear with a crystallographic direction. The point group reduces from D_4, D_6 or D_3 to D_2 or C_2, and the two-dimensional E or E_2 irrep splits into one-dimensional irreps B_2, B_3 or B. This breaks the degeneracy between p_x, p_y or $d_{x^2-y^2}$, d_{xy} pairing functions [Fig. 1(c), left panel], and can be thought of as transiently changing their respective condensation temperatures.

If the system is initially in a state $p_x + ip_y$ with $\mathbf{u} = [0,\ 0,\ 1]^\top$, a linearly-polarized pulse ensures that the chiral form factors $p_x \pm ip_y$ cease to represent eigenstates of the pairing problem for the duration of the pulse due to broken rotation symmetry. Hence, the Bloch vector $\mathbf{u}$ starts to oscillate between nodal p_x and p_y pairing with $\mathbf{u} = [1,\ 0,\ 0]^\top$, $[-1,\ 0,\ 0]^\top$, respectively.

Conversely, a circularly-polarized pump pulse with collinear sample and polarization planes breaks the in-plane mirror symmetries σ_v, σ_d as well as TRS while retaining dis-

crete rotation symmetries, as well as spin-inversion symmetry, or full SU(2) spin rotation symmetry in the absence of spin-orbit coupling. The point group reduces from D_4 to C_4 (or from D_3, D_6 to C_3, C_6 in triangular or hexagonal lattices), and the two-dimensional E irrep splits into chiral complex-conjugate one-dimensional irreps [Fig. 1 (c)]. In this case, the degeneracy of order parameters is lifted in favor of two *chiral* one-dimensional representations $p_x + ip_y$ and $p_x - ip_y$. Analogously, the two-dimensional E or E_2 irrep for d-wave pairing in hexagonal systems reduces to one-dimensional complex-conjugate representations $d_{x^2-y^2} \pm id_{xy}$.

Starting from $p_x + ip_y$, a circularly-polarized pulse will now merely induce oscillations in the gap amplitude Δ while leaving the Bloch vector and chirality of the pairing function inert. If the superconductor is prepared in a nodal state (p_x or p_y), however, p_x and p_y cease to represent eigenstates of the pairing problem due to the circularly polarized laser and the Bloch vector will oscillate between the chiral $p_x + ip_y$ and $p_x - ip_y$ states with $[0,\ 0,\ \pm 1]^\top$. Importantly, while static breaking of rotation symmetries can in principle be achieved via unidirectional strain [27], the requisite joint breaking of mirror and time-reversal symmetries while retaining spin inversion symmetry is possible solely out of equilibrium.

These considerations immediately suggest that arbitrary rotations of the order parameter can be induced by an appropriate sequence of linearly and circularly polarized pulses. Specifically, a domain with reversed chirality [Fig. 1(a)] can be induced by a linearly polarized pulse followed by a circularly polarized pulse, where the handedness of the second pulse is chosen to fix the final handedness of the chiral domain. Once the pulse is switched off, the rotated order parameter remains a steady state of the equilibrium Hamiltonian.

We now apply the above generic mechanism to $d + id$ superconductivity in graphene [6–8, 12, 13] as well as to proposed $p+ip$ triplet superconductivity in Sr_2RuO_4 [15]. We employ an effective honeycomb lattice model of the lowest-energy quasi-flat bands in TBG at $\sim$meV kinetic energy scales [10, 11], as well as an effective three-orbital quasiparticle model for the t_{2g} orbitals in Sr_2RuO_4 with spin-orbit coupling [see Methods]. Since control of the order parameter relies solely on symmetry principles instead of materials specificities, details of the interaction as well as strong-coupling effects and retardation will not qualitatively change the results. Without loss of generality, we therefore start from a mean-field description at low energies with effective attractive nearest-neighbor interactions that stabilize $d_{x^2-y^2} \pm id_{xy}$ and $(p_x \pm ip_y)\hat{\mathbf{z}}$ triplet superconductivity in graphene and Sr_2RuO_4, respectively [see Methods].

The latter is theoretically expected to compete with helical triplet pairing states $p_x\hat{\mathbf{x}}$, $p_y\hat{\mathbf{y}}$ with trivial bulk topology [28]. We emphasize that our proposal permits to distinguish between the two in a pump-probe experiment.

Additionally, optical pumping necessarily heats the superconductor, hence the electronic system must dissipate heat to the substrate and environment in order to return to equilibrium at long times. Since we are primarily interested in the thermalized state *after* the pump instead of details of the relaxation dynamics, the specifics of dissipation are irrelevant. A computationally advantageous choice is to consider tunneling to a wide-band electronic substrate, while ignoring dissipation via electron-phonon coupling. With these considerations, the self-consistent Kadanoff-Baym equations for irradiated chiral superconductors are solved numerically [see Methods].

We first study the order parameter dynamics for a terahertz two-pulse sequence of linearly and circularly polarized pulses, red-detuned from the superconducting gap. The two rows of Fig. 2 depict the time evolution of the superconducting gap magnitude as well as its Bloch vector, starting from a $d_{x^2-y^2} + id_{xy}$ state in graphene, as a function of pump strength. The equilibrium superconducting gap in these simulations is amplified for numerical ease.

As expected from symmetry arguments, the first pulse with linear polarization rotates the Bloch vector from $[0,\ 0,\ 1]^\top$ $(d_{x^2-y^2} + id_{xy})$ towards nodal $d_{x^2-y^2}$ pairing $[1,\ 0,\ 0]^\top$. As sub-gap pumping necessarily heats the superconductor, the gap magnitude is transiently suppressed, but recovers once the system returns to thermal equilibrium via dissipation. Coupling to the extended s-wave pairing channel remains negligible in all parameter regimes studied here. The order parameter dynamics can thus be thought of as effective non-linear dissipative Bloch equations for the Bloch vector. Crucially, the second circularly-polarized pulse triggers a change in chirality beyond a critical pump strength, rotating the order parameter towards $[0,\ 0,\ -1]^\top$ $(d_{x^2-y^2} - id_{xy})$ [right column in Fig. 2]. The chirality of the final state is set by the handedness of the applied circularly-polarized pulse. A pulse of opposite handedness restores the original $d_{x^2-y^2} + id_{xy}$ state.

The second row of Fig. 2 depicts the same pulse sequence, for a three-orbital effective model of the $d_{\mathrm{xz}}, d_{\mathrm{yz}}, d_{\mathrm{xy}}$ orbitals of Sr_2RuO_4. In analogy to $d + id$ superconductivity in graphene, the triplet-paired state rotates from $p + ip$ to $p - ip$ beyond a critical pump strength. We stress that this qualitative universality of the order parameter dynamics highlights the nature of the photo-induced control of chirality as a consequence of selective

symmetry breaking alone, making it applicable to any chiral condensate with spontaneous TRS breaking. Finally, Fig. 2(f) depicts the switching of the qubit Bloch vector as in Fig. 2(c) but represented on the Bloch sphere [see Supplementary Information for a movie of the induced dynamics].

To distinguish the roles of dynamical symmetry breaking and heating, we compared different pulse widths [see Supplementary Information, Fig. S1]. As expected, the superconductor absorbs significantly more energy for a longer pulse, leading to almost complete suppression of the superconducting gap. However, the Bloch vector dynamics remain qualitatively the same. We note that this observation is consistent with expectations from Floquet theory, where dynamical symmetry breaking enters as order $\sim A^2$ or $\sim A^2 t_{\mathrm{hop}}/\Omega$ perturbations to the Hamiltonian that are independent of the transient change of the distribution function. However, the effect persists for few-cycle pulses, well beyond the expected validity of Floquet theory.

Having established a protocol to optically reverse the handedness of a chiral superconductor and associated edge modes, a natural follow-up question is whether such optical control of the order parameter Bloch vector can be truly universal, permitting arbitrary initialization and rotation. To this end, elliptical polarization provides a natural generalization to access the entire state space. Consider a $d+id$ state in graphene, irradiated by a wide high-frequency pulse with polarization Jones vector $\left[\cos\left(\frac{\theta}{2}\right),\ \sin\left(\frac{\theta}{2}\right)e^{i\phi}\right]^{\top}$. Fig. 3 depicts the induced order parameter dynamics and long-time superconducting steady state as a function of polarization vector. Away from linear ($\theta = 0$) or circular ($\theta, \phi = \pi/2$) polarization, the laser pulse now jointly breaks lattice rotation, in-plane mirror and time-reversal symmetries. The transient order parameter eigenstates cease to be $d_{x^2-y^2}$, d_{xy} or $d_{x^2-y^2} \pm id_{xy}$, instead forming a linear superposition that reflects the polarization of the pump. The two angular degrees of freedom of pump pulse polarization thus suffice to permit universal control of the vectorial order parameter. We stress that a generic Bloch vector, deviating from the poles or equator of Fig. 1(b), cannot be realized purely in equilibrium without dynamical control, as any static perturbation that jointly breaks rotation, mirror and time-reversal symmetries would necessarily involve an external magnetic field, quenching the superconducting state.

Beyond direct observation of the induced Majorana edge modes along domain wall boundaries in transport or via spectroscopic methods, one possible experimental confirmation of our predictions follows from noting that the switching from $d+id$ to $d-id$ ($p+ip$ to $p-ip$)

entails a bulk topological transition, necessitating the transient closing of the superconducting gap at discrete points on the Fermi surface. The time-resolved single-particle spectral function and local density of states are particularly simple proxies, measurable in pump-probe angle-resolved photoemission or time-resolved STM with picosecond time resolution for typical switching pulse durations.

Fig. 4 depicts the simulated pump-probe response for $d + id$ pairing in graphene [see Methods]. For terahertz pumping, the local density of states [Fig. 4(b)] exhibits a closing of the single-particle spectral gap near the topological transition between $d + id$ and $d - id$. The corresponding spectral function [Fig. 4(c)] shows the transient breaking of rotation symmetry, with a unidirectional gap closure in the middle panel at the topological transition. The occurrence of a nodal state at the topological transition is partially masked by frequency-shifted side bands as well as transient heating, which uniformly suppresses the superconducting gap.

Conversely, in the high-frequency regime side bands are shifted to high energies and a clean transition from a chiral $d + id$ to a nodal d-wave superconductor and back to a $d - id$ state with opposite chirality is observed [see Fig. 4(d), (e), (f)]. A node appears on the Fermi surface along the $K' \leftrightarrow \Gamma$ cut. Analogously, the local density of states acquires a V-shaped form at the topological transition as expected for a nodal state, before returning to a fully-gapped chiral state. In addition, the extended s-wave pairing symmetry acquires a finite magnitude. However, a transient closing of the single-particle gap remains unavoidable for realizing a topological transition, hence serving as direct evidence of the topological character of the superconducting state.

A direct consequence of our work is the possibility to optically engineer and control arbitrary chiral domains, paving the way to use local optical control of the order parameter to selectively induce or destroy domain-wall Majorana modes. Intriguingly, these could be used to perform topological quantum computation via electrical injection and read-out, in analogy to superconductor - quantum anomalous Hall insulator junctions [29], however with the sequence of braiding operations controlled via the topography of the optically-induced domains. Second, as the presented mechanism relies solely on a two-dimensional irrep of the order parameter, analogous predictions apply to particle-hole condensates such as $d+id$ density waves in hexagonal systems [30]. There, unlike previously-proposed Floquet engineering of topological materials [31–34], our proposal permits ultrafast optical control of

charge-carrying dissipationless chiral edge modes without the problem of runaway heating.

---

[1] Read, N. & Green, D. Paired states of fermions in two dimensions with breaking of parity and time-reversal symmetries and the fractional quantum Hall effect. *Phys. Rev. B* **61**, 10267–10297 (2000).

[2] Schnyder, A. P., Ryu, S., Furusaki, A. & Ludwig, A. W. W. Classification of topological insulators and superconductors in three spatial dimensions. *Phys. Rev. B* **78**, 195125 (2008).

[3] Kallin, C. & Berlinsky, J. Chiral superconductors. *Rep. Prog. Phys.* **79**, 054502 (2016).

[4] Nayak, C., Simon, S. H., Stern, A., Freedman, M. & Sarma, S. D. Non-abelian anyons and topological quantum computation. *Rev. Mod. Phys.* **80**, 1083 (2007).

[5] Sentef, M. A., Tokuno, A., Georges, A. & Kollath, C. Theory of laser-controlled competing superconducting and charge orders. *Phys. Rev. Lett.* **118**, 087002 (2016).

[6] Black-Schaffer, A. M. & Doniach, S. Resonating valence bonds and mean-field d-wave superconductivity in graphite. *Phys. Rev. B* **75**, 134512 (2006).

[7] Nandkishore, R., Levitov, L. & Chubukov, A. Chiral superconductivity from repulsive interactions in doped graphene. *Nat. Phys.* **8**, 158 (2011).

[8] Kiesel, M., Platt, C., Hanke, W., Abanin, D. A. & Thomale, R. Competing many-body instabilities and unconventional superconductivity in graphene. *Phys. Rev. B* **86**, 020507 (2011).

[9] Cao, Y. *et al.* Unconventional superconductivity in magic-angle graphene superlattices. *Nature* **556**, 43–50 (2018).

[10] Bistritzer, R. & MacDonald, A. H. Moiré bands in twisted double-layer graphene. *Proc. Nat. Acad. Sci. USA* **108**, 12233–12237 (2011).

[11] Yuan, N. F. Q. & Fu, L. Model for metal-insulator transition in graphene superlattices and beyond. *Phys. Rev. B* **98**, 045103 (2018).

[12] Liu, C. C., Zhang, L. D., Chen, W. Q. & Yang, F. Chiral SDW and $d + id$ superconductivity in the magic-angle twisted bilayer-graphene. *arXiv:1804.10009* (2018).

[13] Kennes, D. M., Lischner, J. & Karrasch, C. Strong correlations and $d + id$ superconductivity in twisted bilayer graphene. *arXiv:1805.06310* (2018).

[14] Luke, G. M. *et al.* Time-reversal symmetry-breaking superconductivity in Sr_2RuO_4. *Nature*

394, 558–561 (1998).

[15] Mackenzie, A. P. & Maeno, Y. The superconductivity of Sr_2RuO_4 and the physics of spin-triplet pairing. *Rev. Mod. Phys.* **75**, 657–712 (2003).

[16] Elliott, S. R. & Franz, M. Colloquium: Majorana fermions in nuclear, particle, and solid-state physics. *Rev. Mod. Phys.* **87**, 137–163 (2015).

[17] Beenakker, C. W. J. Search for Majorana fermions in superconductors. *Annu. Rev. Cond. Mat. Phys.* **4**, 113–136 (2013).

[18] Alicea, J. New directions in the pursuit of Majorana fermions in solid state systems. *Rep. Prog. Phys.* **75**, 076501 (2012).

[19] Stone, M. & Roy, R. Edge modes, edge currents, and gauge invariance in $p_x + ip_y$ superfluids and superconductors. *Phys. Rev. B* **69**, 184511 (2003).

[20] Ivanov, D. A. Non-Abelian statistics of half-quantum vortices in p-wave superconductors. *Phys. Rev. Lett.* **86**, 268 (2000).

[21] Luke, G. M. *et al.* Muon spin relaxation in UPt_3. *Phys. Rev. Lett.* **71**, 1466–1469 (1993).

[22] Joynt, R. & Taillefer, L. The superconducting phases of UPt_3. *Rev. Mod. Phys.* **74**, 235–294 (2002).

[23] Schmitt, F. *et al.* Transient electronic structure and melting of a charge density wave in $TbTe_3$. *Science* **321**, 1649–1652 (2008).

[24] Fausti, D. *et al.* Light-induced superconductivity in a stripe-ordered cuprate. *Science* **331**, 189–191 (2011).

[25] Mitrano, M. *et al.* Possible light-induced superconductivity in K_3C_{60} at high temperature. *Nature* **530**, 461–464 (2016).

[26] Sigrist, M. & Ueda, K. Phenomenological theory of unconventional superconductivity. *Rev. Mod. Phys.* **63**, 239–311 (1991).

[27] Hicks, C. W. *et al.* Strong increase of tc of Sr_2RuO_4 under both tensile and compressive strain. *Science* **344**, 283–285 (2014).

[28] Scaffidi, T., Romers, J. C. & Simon, S. H. Pairing symmetry and dominant band in Sr_2RuO_4. *Phys. Rev. B* **89**, 220510 (2013).

[29] Lian, B., Sun, X.-Q., Vaezi, A., Qi, X.-L. & Zhang, S.-C. Topological quantum computation based on chiral Majorana fermions. *Proc. Nat. Acad. Sci. USA*, adv. online pub. *DOI: 10.1073/pnas.1810003115* (2018).

[30] Nayak, C. Density wave states of non-zero angular momentum. *Phys. Rev. B* **62**, 4880 (2000).

[31] Kitagawa, T., Oka, T., Brataas, A., Fu, L. & Demler, E. Transport properties of nonequilibrium systems under the application of light: Photoinduced quantum hall insulators without landau levels. *Phys. Rev. B* **84**, 235108 (2011).

[32] Lindner, N. H., Refael, G. & Galitski, V. Floquet topological insulator in semiconductor quantum wells. *Nature Phys.* **7**, 490–495 (2011).

[33] Claassen, M., Jia, C., Moritz, B. & Devereaux, T. P. All-optical materials design of chiral edge modes in transition-metal dichalcogenides. *Nature Comm.* **7**, 13074 (2016).

[34] Hübener, H., Sentef, M. A., Giovannini, U. D., Kemper, A. F. & Rubio, A. Creating stable Floquet-Weyl semimetals by laser-driving of 3D Dirac materials. *Nat. Commun.* **8**, 13940 (2016).

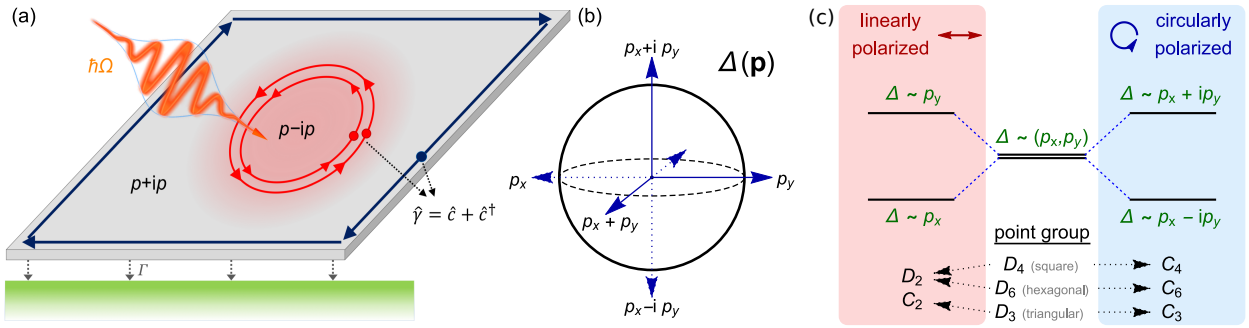

Figure 1. **Driven chiral superconductors and dynamical symmetry breaking of two-dimensional order parameters.** (a) Schematic of a photo-induced domain with opposite chirality in a $p + ip$ superconductor. Induced domain walls host two chiral Majorana edge modes (red arrows in a), and persist after the pump is off, while the system equilibrates locally by dissipating energy with rate Γ. (b) Bloch vector representation of the non-equilibrium pairing function of a chiral superconductor. Optical pumping induces arbitrary rotations of the order parameter vector via choice of polarization. (c) Irradiation with linearly-polarized light breaks the discrete lattice rotation symmetry, lifting the degeneracy between p_x, p_y order parameters. Circularly-polarized light breaks both the coplanar reflection symmetries and time-reversal, splitting the degeneracy into conjugate chiral representations $p_x \pm ip_y$.

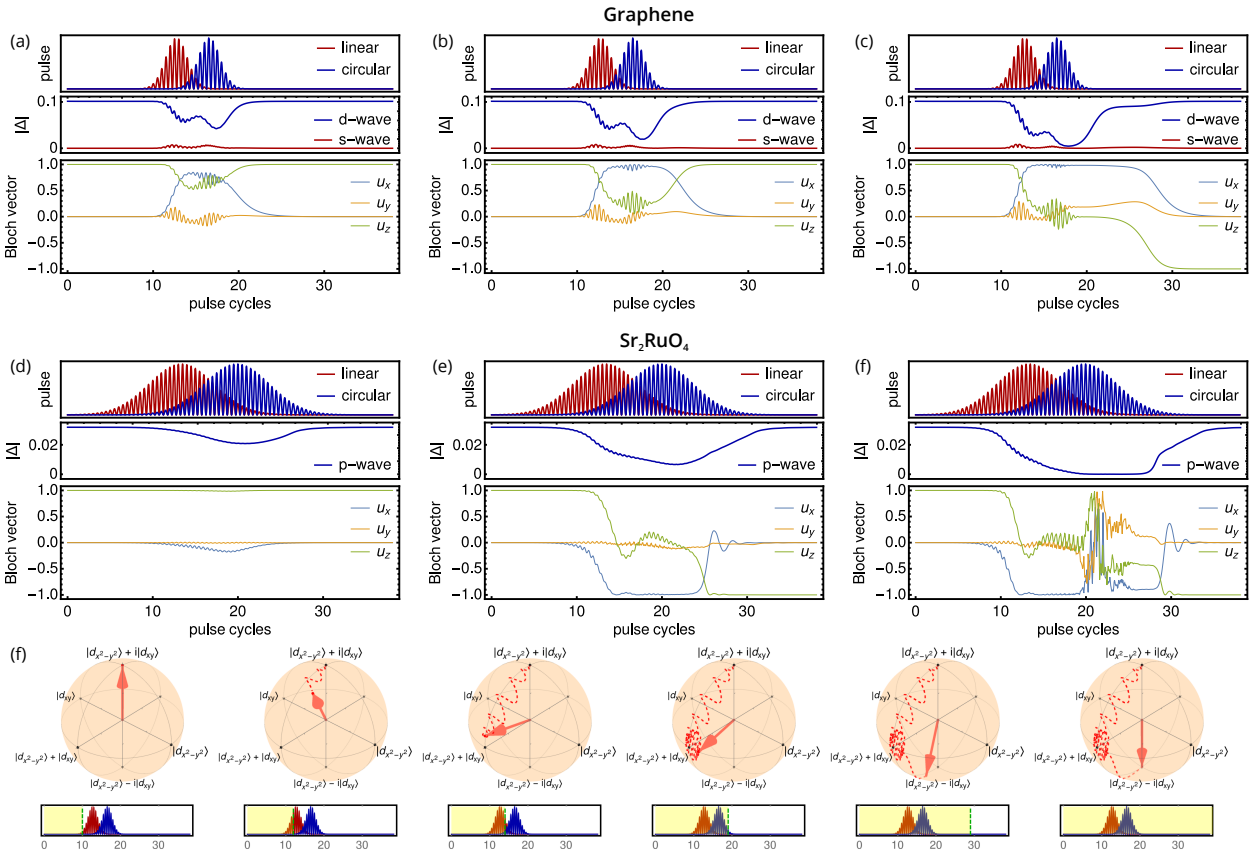

Figure 2. **Ultrafast Control of Chirality of the Superconducting Order Parameter.** Evolution of the Bloch vector and magnitude of the superconducting gap, for an ultrafast two-pulse sequence with linear and circular polarization, as a function of pump strength. Top row depicts the order parameter dynamics starting from a $d_{x^2-y^2} + id_{xy}$ state in graphene, for dimensionless pump strengths $A = 0.25, 0.35, 0.4$, from left to right, for $\omega = 0.8\Delta_{\text{eq}}$ and a short pulse envelope. The linearly-polarized pulse rotates the Bloch vector from $[0,\ 0,\ 1]^\top$ to a nodal state with $[0,\ 1,\ 0]$; the second circularly-polarized pulse selects a state with opposite chirality $[0,\ 0,\ -1]^\top$ beyond a critical pump strength. Weak coupling to extended s-wave pairing is allowed via symmetry but negligible in the parameter regimes considered here. Middle row depicts the optical reversal of chirality from $p_x + ip_y$ to $p_x - ip_y$ in an effective three-band model for Sr_2RuO_4, for $A = 0.1, 0.2, 0.3$ from left to right. (f) Switching of the qubit Bloch vector as in (c) but represented on the Bloch sphere (see supplemental information for the corresponding movie). Reversal of chirality remains insensitive to small variations of pulse distance or widths [Supplementary Information, Sec. I].

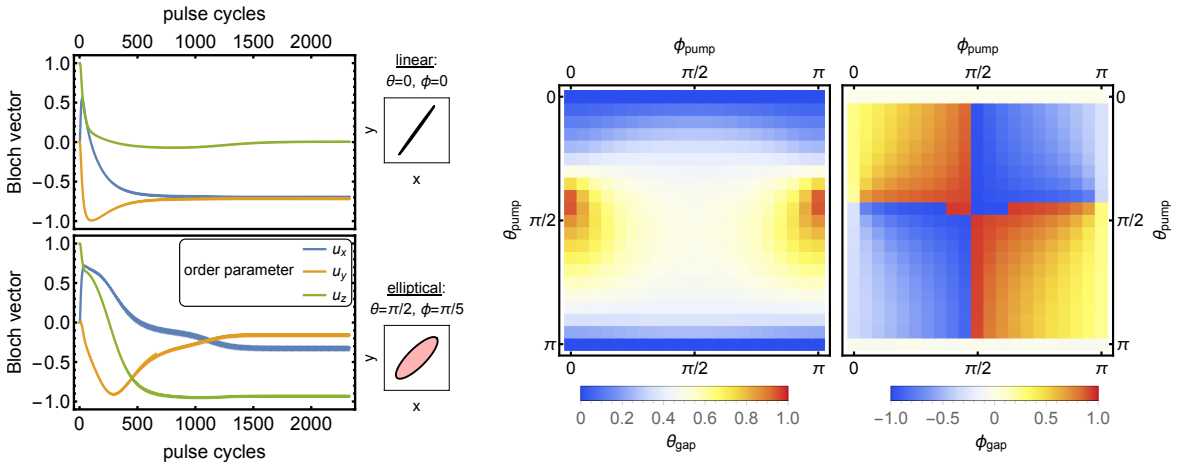

Figure 3. **Universal control of chiral superconductors.** Left: Time evolution and steady states for a high-frequency wide envelope pump pulse, starting from a $d + id$ state in graphene, for linear (top panel) and elliptical (bottom panel) polarization. The polarization ellipses are depicted as insets. Right: Dependence of the steady-state order parameter Bloch vector $\mathbf{\Delta} = \left[\cos(\theta_{\rm gap}/2),\ \sin(\theta_{\rm gap}/2)e^{i\phi_{\rm gap}}\right]^\top$ on the choice of elliptical pump polarization, expressed via a Jones vector $[\cos(\theta_{\rm pump}/2),\ \sin(\theta_{\rm pump}/2)e^{i\phi_{\rm pump}}]^\top$. Linear-horizontal and circular polarization correspond to $\theta = 0$ and $\theta = \pi/2, \phi = \pi/2$, respectively. Each data point is computed as the time-evolved steady state, starting from a $d + id$ state. A simple physical picture emerges via noting that a generic elliptically-polarized pulse can always be represented as a superposition of pulses with linear and circular polarization; however, whereas rotational symmetry breaking due to linear polarization is proportional to the square of the field strength $\sim A^2$, the magnitude of mirror and time-reversal symmetry breaking is proportional to $\sim A^2/\Omega$. The relative strength of symmetry-breaking perturbations subsequently determines the order parameter steady state. We note that a generic Bloch vector, deviating from the poles or equator of Fig. 1(b), cannot be realized purely in equilibrium without dynamical control, as any perturbation that jointly breaks rotation, mirror and time-reversal symmetries would necessarily involve an external magnetic field, quenching the superconducting state.

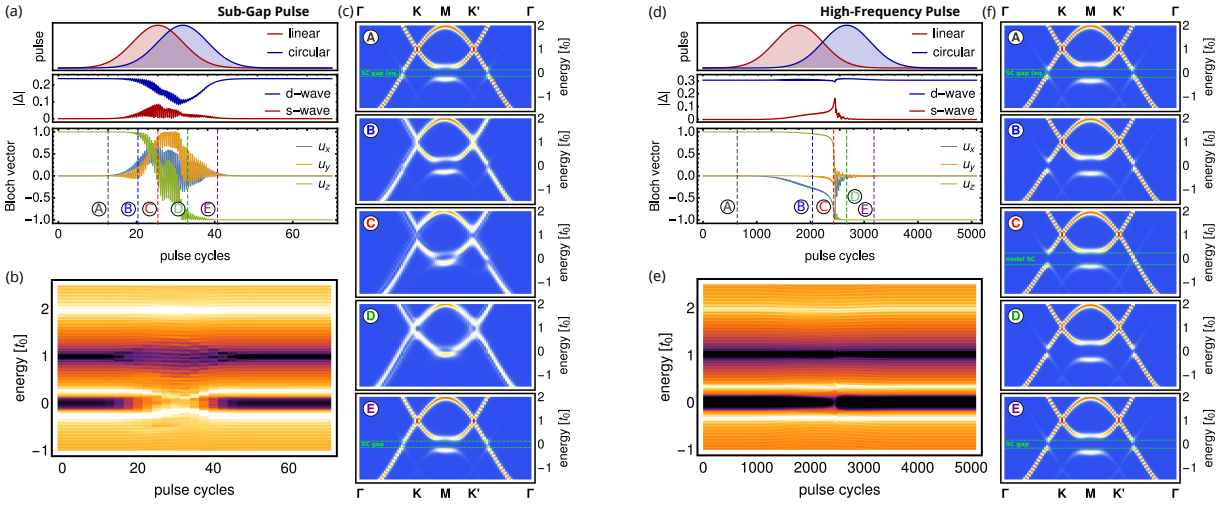

Figure 4. **Pump-probe measurement of order parameter dynamics.** Order parameter evolution [(a), (d)], time-dependent local density of states [(b), (e)], and time-resolved spectral functions [(c), (f)], for a two-pulse sequences that reverses the chirality of a $d+id$ state in graphene. Left and right panels depict sub-gap ($\omega = 0.18t_{\rm hop}$) and high-frequency pumping ($\omega = 8.0t_{\rm hop}$), respectively. Transient spectral functions (c), (f) are depicted for time slices indicated in (a), (d), for a probe pulse width of $\sigma_{\rm probe} = 10$ [see main text]. Density of states and spectral functions [see Methods] depict symmetry breaking and closing of the single-particle gap. For high-frequency pumping, a nodal state becomes cleanly visible along the $\Gamma \to K'$ cut at the topological transition between $d+id$ and $d-id$, with a V-shaped local density of states. In general, transiently-induced nodes of the superconducting gap are not constrained to lie on high-symmetry cuts, requiring a mapping of the entire Fermi surface.

METHODS

Details of Graphene Calculation A decade after first proposals that electronic interactions in heavily-doped monolayer graphene can induce effective attractive pairing for chiral d-wave superconductivity at low energies [6–8], experiments found evidence of superconductivity in gated TBG at magic twist angles [11]. Among a host of proposed theories, the common theme is that if the superconducting state indeed derives from repulsive electronic interactions in a flat band, then the dominant instability should be chiral pairing in the d-wave channel [12, 13, 34–39], although other mechanisms such as standard electron-phonon coupling have been proposed as well [40, 41].

Following Refs. [10, 11], the lowest-energy quasi-flat bands in TBG can be captured via an effective two-orbital honeycomb lattice model at $\sim$meV kinetic energy scales.

$$\hat{H} = -\sum_{\substack{nn' \\ \alpha\alpha'\sigma}} t_{nn'}^{\alpha\alpha'}\ \hat{c}^{\dagger}_{n\alpha\sigma}\hat{c}_{n'\alpha'\sigma} - \mu\sum_{i\alpha\sigma}\hat{n}_{i\alpha\sigma} \tag{A.1}$$

where α, α' and σ denote orbital and spin indices. Upon neglecting weak breaking of SU(4) sublattice symmetry [13], $t_{nn'}^{\alpha\alpha'} \neq 0$ only for nearest-neighbor hopping between the same orbitals, and mean field theory for effective renormalized interactions becomes identical to monolayer graphene doped to the van-Hove singularity [7, 8], but with an additional orbital degree of freedom.

Since control of the order parameter relies solely on symmetry principles instead of materials specificities, microscopic details of the interaction as well as strong-coupling effects and retardation should not qualitatively change the results. Without loss of generality, we therefore constrain our simulations to nearest-neighbor attractive interactions $V_{\mathbf{q}} = -V\gamma_{\mathbf{q}}\hat{\tau}^{+}$+h.c. that are orbitally isotropic, with

$$\gamma_{\mathbf{k}} = 1 + e^{-i(k_x/2-\sqrt{3}k_y/2)} + e^{+i(k_x/2+\sqrt{3}k_y/2)} \tag{A.2}$$

and $\hat{\tau}^{+} \equiv \hat{\tau}^{x} + i\hat{\tau}^{y}$ the sublattice Pauli matrices. Such interactions stabilize $d_{x^2-y^2}$ and d_{xy} pairing with

$$\hat{\eta}^{(1)}_{\mathbf{k}} = \frac{1}{\sqrt{6}}\left[2 - e^{i(k_x/2-\sqrt{3}k_y/2)} - e^{-i(k_x/2-\sqrt{3}k_y/2)}\right]\hat{\tau}^{+} + \text{h.c.} \tag{A.3}$$

and

$$\hat{\eta}^{(2)}_{\mathbf{k}} = \frac{1}{\sqrt{2}}\left[e^{i(k_x/2-\sqrt{3}k_y/2)} - e^{-i(k_x/2-\sqrt{3}k_y/2)}\right]\hat{\tau}^{+} + \text{h.c.}, \tag{A.4}$$

that span the basis for the order parameter Bloch vector. Furthermore, extended s-wave pairing with

$$\hat{\eta}^{(s)}_{\mathbf{k}} = \frac{1}{\sqrt{3}} \left[1 + e^{i(k_x/2 - \sqrt{3}k_y/2)} + e^{-i(k_x/2 - \sqrt{3}k_y/2)} \right] \hat{\tau}^{+} + \text{h.c.} \tag{A.5}$$

is permitted by symmetry but suppressed in equilibrium. This choice of $V_{\mathbf{q}}$ matches expectations for renormalized interactions from functional renormalization group calculations [13].

The pump field enters via Peierls substitution, with hopping amplitudes $t_{nn'} \to t_{nn'} e^{i \int_{n'}^{n} d\mathbf{r} \cdot \mathbf{A}(t)}$. The dimensionless peak pulse strengths quoted in the main text relate to the electric field $\mathcal{E}$ via $A = a_0 e \mathcal{E}/(\hbar\Omega)$, where a_0, e are the lattice constant and electric charge, respectively. The order parameter simulations for graphene in the main text were performed for $V = -0.621$, $\mu = -0.95$, $\Gamma = 0.05$ at bath temperature $T = 0.1$, yielding an equilibrium gap of $\Delta \sim 0.1$, all in units of nearest-neighbor hopping t_{hop}. Temperature, relaxation constant and superconducting gap are all exaggerated to ease numerical simulations. High-frequency simulations were performed for pump frequencies of 1.3 times the electronic bandwidth. Simulations of the pump-probe response were performed for $T = 0.05$, $\Gamma = 0.01$ and $V = -0.067$, at signficantly increased numerical cost.

Details of Sr_2RuO_4 Calculation To emphasize the universality of the order parameter dynamics, we additionally study the evolution of the chiral gap function in a low-energy quasi-particle model of Sr_2RuO_4. We employ a three orbital tight-binding model of maximally-localized Wannier functions [42] constructed for the Ru-4d t_{2g} subspace from a non-spin-polarized density functional calculation (using Wien2k [43] with PBE functional [44], wien2wannier [45] and wannier90 [46]). The local self-energy is obtained in the normal state (at 29K) with dynamical mean-field theory [47] using the TRIQS toolbox [48–50]. Additionally, we add a single particle spin-orbit term with an enhanced coupling constant of 200meV. This choice is based on theoretical studies [51, 52] and justified by an in-depth analysis of high-precision angle-resolved photo-emission measurements [53]. In the latter, details of the model and dynamical mean-field theory calculation are presented. A two-dimensional quasi-particle model is derived via linearization of the self-energy at the Fermi surface. This effective model describes quasi-particles in a $\sim \pm 30$meV energy range around the Fermi energy, hence underestimating the overall electronic bandwidth. However, we expect that, for our purposes, this is not pertinent to the two off-resonant regimes under consideration. For sub-gap pumping, the time evolution can be expected to be sensitive only

to states in the vicinity of the Fermi energy, whereas the high-frequency Floquet regime is essentially adiabatic, with the bare bandwidth W disappearing as a relevant energy scale provided that the frequency $\Omega \gg W$.

With these considerations in mind, we truncate the effective quasiparticle tight-binding model beyond 10^{th}-nearest neighbor hopping:

$$\mathbf{H}_{\mathbf{k}} = \begin{bmatrix} \mathbf{h}_{\mathbf{k},+} & 0 \\ 0 & \mathbf{h}_{\mathbf{k},-} \end{bmatrix}, \quad \mathbf{h}_{\mathbf{k},\nu} = \begin{bmatrix} \epsilon^{\text{xz}}_{\mathbf{k}} & -i\nu\lambda + g_{\mathbf{k}} & i\lambda \\ i\nu\lambda + g_{\mathbf{k}} & \epsilon^{\text{yz}}_{\mathbf{k}} & -\nu\lambda \\ -i\lambda & -\nu\lambda & \epsilon^{\text{xy}}_{\mathbf{k}} \end{bmatrix} \tag{A.6}$$

with $\nu = \pm$, where λ is the renormalized spin-orbit coupling constant. The kinetic matrix elements and the corresponding Fermi surface depicting the orbital character of the individual sheets are provided in the Supplementary Information, section III.

The tight-binding model transforms under the point group $\text{D}_{4\text{h}}$, and hence has a degeneracy (two-fold irreducible representation E_{u}) between triplet $p_x\hat{\mathbf{z}}$, $p_y\hat{\mathbf{z}}$ states, where $\mathbf{z}$ refers to the Pauli matrix in the usual triplet channel spinor representation. It is invariant under inversions, as well as C_4 rotations. For the main text, we consider an attractive interaction in the $(p_x + ip_y)\hat{\mathbf{z}}$ pairing channel. We note that while the nature of the superconducting order is under active investigation [54], chiral pairing can be distinguished from competing proposals in a pump-probe experiment as shown in the main text. Further symmetry considerations are deferred to the Supplementary Information.

Details of the Order Parameter Evolution We start from the self-consistent Kadanoff-Baym equations for the Green's function $\mathcal{G}$ in Keldysh-Nambu basis

$$i\partial_t \mathcal{G}_{\mathbf{k}}(t,t') = \mathcal{H}_{\mathbf{k}}(t, \mathbf{\Delta}_{\mathbf{k}}(t))\ \mathcal{G}_{\mathbf{k}}(t,t') + \int d\tau\ \hat{\Sigma}_{\mathbf{k}}(t,\tau)\ \mathcal{G}_{\mathbf{k}}(\tau,t') \tag{A.7}$$

$$\mathbf{\Delta}_{\mathbf{k}}(t) = \frac{1}{L}\sum_j v^{(j)} \hat{\boldsymbol{\eta}}^{(j)}_{\mathbf{k}} \sum_{\substack{\mathbf{k}' \\ \alpha\beta}} \hat{\eta}^{(j)}_{\mathbf{k}'\alpha\beta} \left\langle \hat{c}_{-\mathbf{k}',\beta\downarrow} \hat{c}_{\mathbf{k}',\alpha\uparrow} \right\rangle \tag{A.8}$$

and solve the resulting integro-differential equations of motion on a 60×60 momentum point grid with a time step no larger than $1/40$ of the pump period. Here, $\mathcal{G}_{\mathbf{k}}(t,t')$ is the Keldysh-Nambu Green's function, $\mathcal{H}_{\mathbf{k}}(t, \mathbf{\Delta}_{\mathbf{k}}(t))$ denotes a multi-band Bogoliubov de Gennes Hamiltonian, and the pump field couples to electrons via Peierls substitution. Attractive interactions are treated in an instantaneous mean field approximation for the superconducting multi-band order parameter $\mathbf{\Delta}_{\mathbf{k}}$, with orbital indices denoted by α, β, and where

$v^{(j)}$ denotes the decomposition of two-body interaction matrix elements in terms of form factors $\hat{\eta}_{\mathbf{k}}^{(j)}$ for the relevant irreducible representations, indexed by j. Finally, the self energy $\hat{\Sigma}$ models weak dissipative coupling to a metallic substrate. In the wide-band limit for the bath, this corresponds to a retarded self energy $\Sigma^R(t,t') = -i\Gamma\ \delta(t-t')$ and Keldysh self-energy $\Sigma^K(t,t') = -2\Gamma\ T\left[\sinh(\pi(t-t')T)\right]^{-1}$, with Γ and T the effective relaxation constant and substrate equilibrium temperature, respectively. Further details can be found in the Supplementary Information, section IV.

Details of the $\rho(\omega,T)$ and $A_{\mathbf{k}}(\omega,T)$ Calculation We calculate the time-resolved local density of states

$$\rho(\omega,T) = 2\mathrm{Im}\int d\tau\ e^{-i\omega\tau}\,\mathrm{Tr}\,\mathbf{G}^R(T+\tau/2,T-\tau/2) \tag{A.9}$$

as well as the probe-averaged single-particle spectral function

$$A_{\mathbf{k}}(\omega,T) = \int dt_1 dt_2\ e^{-i\omega(t_1-t_2)}s(t_1)s(t_2)\,\mathrm{Tr}\,\mathbf{G}^R(t_1,t_2) \tag{A.10}$$

using a Gaussian probe pulse shape function $s(\tau) = e^{-(\tau-T)^2/(2\sigma_{\mathrm{probe}})}$ and where $\mathbf{G}^R$ denotes the retarded Green's function. We employ a momentum grid with 90×90 points, and the equilibrium superconducting gap is exaggerated to ease the computational cost without changing the qualitative behavior.

BIBLIOGRAPHY – METHODS

[34] Xu, C. & Balents, L. Topological superconductivity in twisted multilayer graphene. *Phys. Rev. Lett.* **121**, 087001 (2018).

[35] Dodaro, J. F., Kivelson, S. A., Schattner, Y., Sun, X. Q. & Wang, C. Phases of a phenomenological model of twisted bilayer graphene. *Phys. Rev. B* **98**, 075154 (2018).

[36] Guo, H., Zhu, X., Feng, S. & Scalettar, R. T. Pairing symmetry of interacting fermions on twisted bilayer graphene superlattice. *Phys. Rev. B* **97**, 235453 (2018).

[37] Huang, T., Zhang, L. & Ma, T. Antiferromagnetically ordered Mott insulator and $d+id$ superconductivity in twisted bilayer graphene: A quantum Monte Carlo study. *arXiv:1804.06096* (2018).

[38] Po, H. C., Zou, L., Vishwanath, A. & Senthil, T. Origin of Mott insulating behavior and superconductivity in twisted bilayer graphene. *arXiv:1803.09742* (2018).

[39] Isobe, H., Yuan, N. F. Q. & Fu, L. Unconventional superconductivity and density waves in twisted bilayer graphene. *arXiv:1805.06449* (2018).

[40] Padhi, B., Setty, C. & Phillips, P. W. Doped twisted bilayer graphene near magic angles: Proximity to Wigner crystallization not Mott insulation. *arXiv:1804.01101* (2018).

[41] Lian, B., Wang, Z. & Bernevig, B. A. Twisted bilayer graphene: A phonon driven superconductor. *arXiv:1807.04382* (2018).

[42] Souza, I., Marzari, N. & Vanderbilt, D. Maximally localized Wannier functions for entangled energy bands. *Phys. Rev. B* **65**, 035109 (2001).

[43] Blaha, P., Schwarz, K., Madsen, G., Kvasnicka, D. & Luitz, J. *WIEN2k, An augmented Plane Wave + Local Orbitals Program for Calculating Crystal Properties* (Techn. Universitat Wien, Austria, ISBN 3-9501031-1-2., 2001).

[44] Perdew, J. P., Burke, K. & Ernzerhof, M. Generalized gradient approximation made simple. *Phys. Rev. Lett.* **77**, 3865–3868 (1996).

[45] Kuneš, J. *et al.* Wien2wannier: From linearized augmented plane waves to maximally localized Wannier functions. *Comput. Phys. Commun.* **181**, 1888 – 1895 (2010).

[46] Mostofi, A. A. *et al.* wannier90: A tool for obtaining maximally-localised Wannier functions. *Comput. Phys. Commun.* **178**, 685 – 699 (2008).

[47] Georges, A., Kotliar, G., Krauth, W. & Rozenberg, M. J. Dynamical mean-field theory of strongly correlated fermion systems and the limit of infinite dimensions. *Rev. Mod. Phys.* **68**, 13–125 (1996).

[48] Parcollet, O. *et al.* Triqs: A toolbox for research on interacting quantum systems. *Comput. Phys. Commun.* **196**, 398 – 415 (2015).

[49] Seth, P., Krivenko, I., Ferrero, M. & Parcollet, O. Triqs/cthyb: A continuous-time quantum monte carlo hybridisation expansion solver for quantum impurity problems. *Comput. Phys. Commun.* **200**, 274 – 284 (2016).

[50] Aichhorn, M. *et al.* Triqs/dfttools: A triqs application for ab initio calculations of correlated materials. *Comp. Phys. Comm.* **204**, 200 – 208 (2016).

[51] Zhang, G., Gorelov, E., Sarvestani, E. & Pavarini, E. Fermi surface of Sr_2RuO_4: Spin-orbit and anisotropic coulomb interaction effects. *Phys. Rev. Lett.* **116**, 106402 (2016).

[52] Kim, M., Mravlje, J., Ferrero, M., Parcollet, O. & Georges, A. Spin-orbit coupling and electronic correlations in Sr_2RuO_4. *Phys. Rev. Lett.* **120**, 126401 (2018).

[53] Tamai, A. *et al. to be published* .

[54] Mackenzie, A. P., Scaffidi, T., Hicks, C. W. & Maeno, Y. Even odder after twenty-three years: the superconducting order parameter puzzle of Sr_2RuO_4. *Nature Quantum Mater.* **2**, 40 (2017).

ACKNOWLEDGMENTS

We gratefully thank Antoine Georges and Andrew J. Millis for helpful discussions. M.C. and M.Z. are supported by the Flatiron Institute, a division of the Simons Foundation. D.M.K. and M.A.S. acknowledge support from the DFG through the Emmy Noether program (KA 3360/2-1 and SE 2558/2-1, respectively). We acknowledge financial support from the European Union Horizon 2020 research and innovation program under the European Research Council (ERC Advanced Grant Agreement no. 69409).

Competing financial interests: The authors declare no competing financial interests.

Corresponding author Martin Claassen (mclaassen@flatironinstitute.org).

Data availability: All data generated and analyzed during this study are available from the corresponding author upon request.

SUPPLEMENTARY INFORMATION

1. Pump Envelope Dependence

Here, we briefly discuss the dependence of the chiral order parameter dynamics on the width of the pump pulse. As discussed in the main text, the ensuing dynamical symmetry-breaking is best understood in the Floquet limit of wide envelope pulses, however optical reversal of chirality similarly happens for ultrafast optical pulses.

It is therefore desirable to demonstrate that the dynamics in both limits are qualitatively equivalent. Fig. S1 depicts the dynamics of the gap magnitude and Bloch vector for a driven $d + id$ superconductor in graphene, as a function of pulse width. One finds that the superconducting gap magnitude is quenched for increasing pulse widths [top to bottom rows], however the dynamics of the Bloch vector are largely unaffected, instead depending

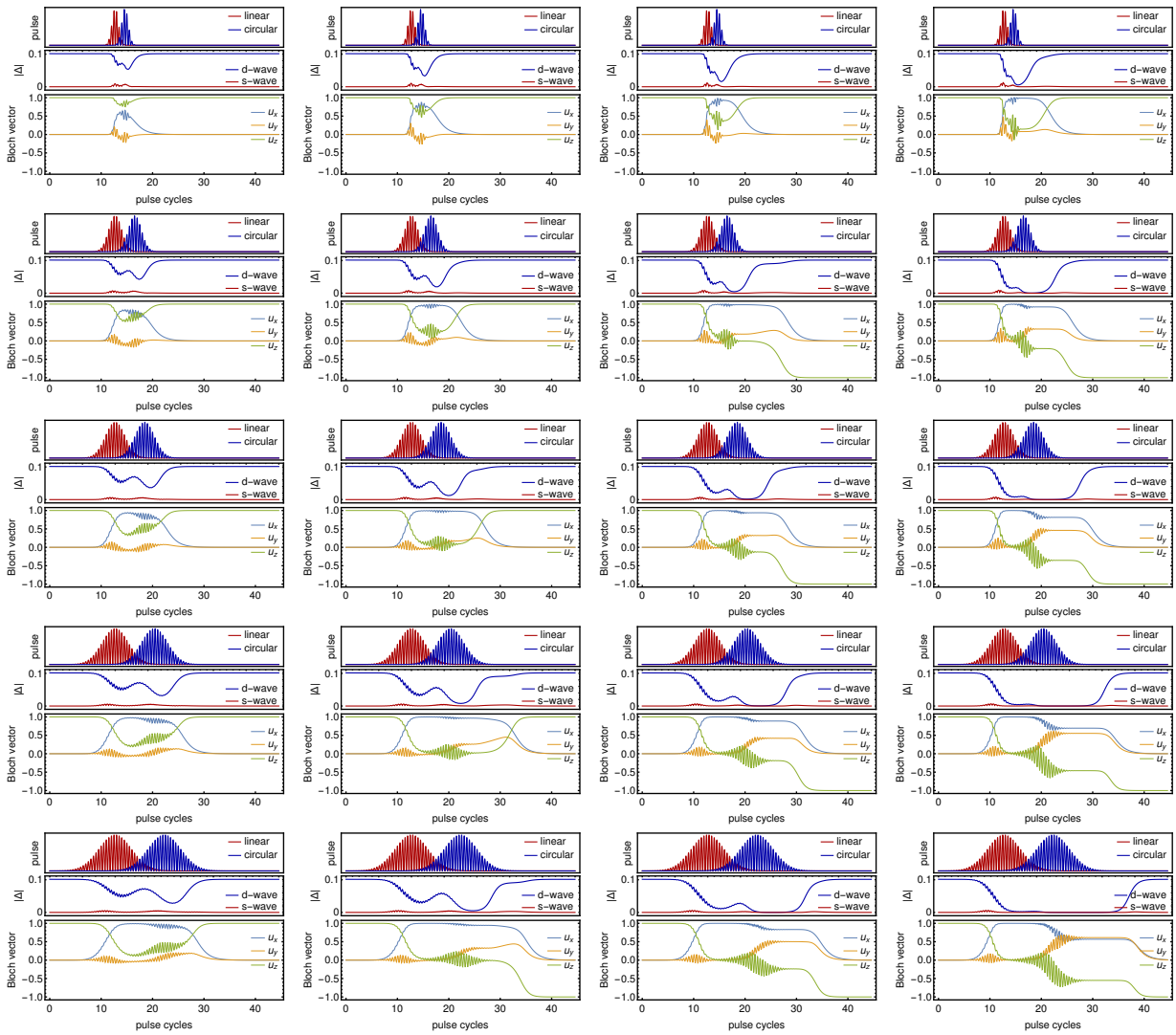

Figure S1. **Pulse width dependence of order parameter dynamics.** Order parameter dynamics for a $d + id$ superconductor in graphene as a function of increasing pulse width with $\Omega = 0.8|\Delta|(t = 0)$, from top to bottom [depicted in the top sub-panels], and pump strength $A = 0.25, 0.3, 0.35, 0.4$, from left to right. Increasing the pulse width increases energy absorption and subsequently quenches superconducting order. Conversely, symmetry breaking and Bloch vector dynamics are largely independent of pulse width.

solely on the peak field strength [left to right columns].

Remarkably, the dependence on peak field strength corresponds precisely to expectations for the Floquet limit of wide pump pulses, carried over to ultrafast time scales. In the Floquet limit, the pulse can be viewed as a dynamical perturbation to the kinetic Hamiltonian.

Here, dynamical reduction of the discrete lattice rotation symmetry generically enters as a perturbation proportional to $\sim [\mathcal{J}_0(A) - 1]$ the zeroth Bessel function, quadratic in the peak field strength at weak fields [S1]. Similarly, dynamical breaking of time-reversal symmetry appears as a perturbation $\sim [\mathcal{J}_1(A)]^2/\Omega$, again quadratic in the peak field strength while simultaneously sensitive to the pump frequency [S2]. Conversely, the quenching of the superconducting gap for wider pulse envelopes can be understood as a heating effect.

2. Chirality Reversal in the High-Frequency Regime

Analogous to the discussion of sub-gap pumping in the main text, a sequence of linearly-polarized and circularly-polarized high-frequency pulses lead to a controlled reversal of the chirality of the superconducting order. Fig. S2(a) depicts a $d + id$ superconducting state in graphene, doped close to the van Hove singularities with $\mu = -0.95t_{\text{hop}}$, and driven with a wide-envelope pulse with linear polarization along x.

At high frequency $\Omega = 10t_{\text{hop}}$, the pulse transiently quenches hopping along the x direction proportional to the zeroth Bessel function of pump strength $\mathcal{J}_0(A)$, unidirectionally increasing the density of states at the Fermi level and breaking the lattice rotation symmetry. The $d + id$ state ceases to represent a steady state of the system, and the pulse rotates from $d + id$ to $d_{x^2-y^2}$ beyond a critical field strength. Fig. S2(b) depicts the analogous scenario of a $d_{x^2-y^2}$ state pumped with a wide envelope pulse with circular polarization. Here, breaking of time-reversal and in-plane mirror symmetries is proportional to $\mathcal{J}_1(A)/\Omega$, and the steady state is a $d \pm id$ state, with its chirality determined by the handedness of the pump pulse. Coupling to an extended s-wave state state is negligible for sufficiently smooth pump envelopes, and s-wave pairing does not become an accessible steady state solution over all investigated parameter regimes.

Consequently, the chirality of a $d + id$ state can be inverted by a two-pulse sequence of a linearly-polarized pulse that stabilizes a $d_{x^2-y^2}$ state, followed by a circularly-polarized pulse of appropriate handedness [Fig. S2(c)]. Analogously, Fig. S2(d) depicts a driven $\sin(k_x) + i\sin(k_y)$ triplet state in a single-band superconductor on the square lattice. Here, dynamical breaking of time-reversal symmetry is a higher-order effect in A – an artifact of a single-band model – nevertheless, rotation of the chirality of the order parameter proceeds analogously.

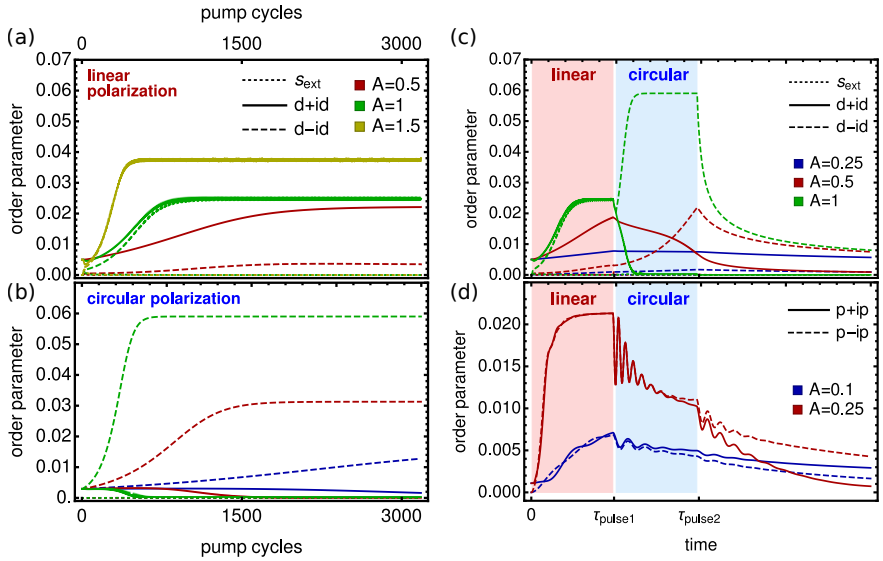

Figure S2. **Floquet reversal of the chirality of the order parameter in the high-frequency regime.** (a) and (b) depict wide-pulse Floquet steady states for ω greater than the electronic band width, for $d_{x^2-y^2} + id_{xy}$ superconductivity in graphene. The depicted order parameters correspond to the z-component of the Bloch vector scaled by the gap magnitude. Linear polarization [(a)] drives the superconductor into a nodal p_x steady state, whereas circular polarization [(b)] rotates a p_x state into a state with $p_x \pm ip_y$ pairing. (c) A two-pulse sequence of a linearly-polarized followed by a circularly-polarized pulse in the Floquet regime can reverse the chirality of the order parameter. (d) The same two-pulse sequence for a single-band square lattice model with $\sin(k_x) \pm i \sin(k_y)$ triplet pairing, similarly inducing a reversal of chirality.

3. Low-Energy Model for the d_{xz}, d_{yz}, d_{xy} orbitals of Sr_2RuO_4

As discussed in the Methods section of the main text, we employ an effective two-dimensional three-orbital model of Sr_2RuO_4. Taking into account solely atomic spin-orbit coupling, symmetry considerations constrain the quasi-particle Hamiltonian to

$$\mathbf{H_k} = \begin{bmatrix} \mathbf{h}_{\mathbf{k},+} & 0 \\ 0 & \mathbf{h}_{\mathbf{k},-} \end{bmatrix} \tag{S1}$$

with

$$\mathbf{h}_{\mathbf{k},\nu} = \begin{bmatrix} \epsilon^{\mathrm{xz}}_{\mathbf{k}} & -i\nu\lambda + g_{\mathbf{k}} & i\lambda \\ i\nu\lambda + g_{\mathbf{k}} & \epsilon^{\mathrm{yz}}_{\mathbf{k}} & -\nu\lambda \\ -i\lambda & -\nu\lambda & \epsilon^{\mathrm{xy}}_{\mathbf{k}} \end{bmatrix} \tag{S2}$$

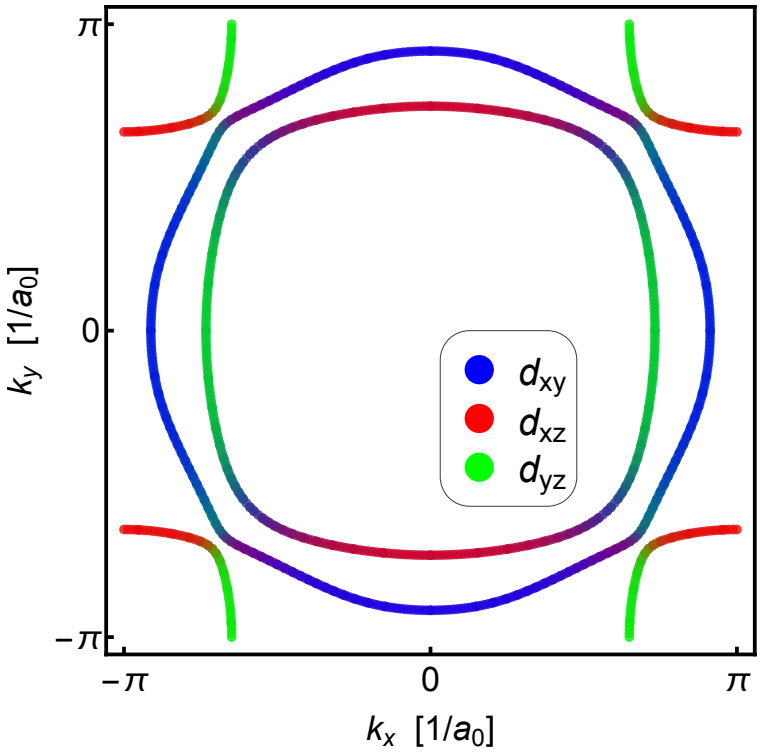

Figure S3. **Fermi surface and orbital character of Sr_2RuO_4.** Fermi surface and d_{xy}, d_{xz}, d_{yz} orbital components, calculated from the effective quasi-particle tight-binding model of Eq. (S1). The inclusion of spin-orbit coupling has a strong influence on the topography of the Fermi surface and also leads to a mixing of orbital characters along the individual sheets. The Fermi surface of this model is in excellent agreement with high-precision angle-resolved photo-emission data [S3].

Here we give the kinetic matrix elements used in the main text:

$$\begin{aligned}\epsilon^{\mathrm{xz}}_{\mathbf{k}} &= -0.109297 - 0.034634\cos(k_x) - 0.195441\cos(k_y) + 0.023565\cos(2k_y)\\ &+ 0.001559\left[\cos(k_x-3k_y)+\cos(k_x+3k_y)\right] + 0.006043\left[\cos(k_x-2k_y)+\cos(k_x+2k_y)\right]\\ &+ 0.002895\left[\cos(k_x-k_y)+\cos(k_x+k_y)\right] + 0.001013\left[\cos(2k_x-k_y)+\cos(2k_x+k_y)\right]\\ &+ 0.002835\cos(2k_x) + 0.002595\cos(3k_y) \end{aligned} \tag{S3}$$

$$\epsilon^{\mathrm{yz}}_{\mathbf{k}} = \epsilon^{\mathrm{xz}}_{(k_y,-k_x)} \tag{S4}$$

$$\begin{aligned}\epsilon^{\mathrm{xy}}_{\mathbf{k}} &= -0.074803 - 0.134663\left[\cos(k_y)+\cos(k_x)\right] + 0.001638\left[\cos(2k_y)+\cos(2k_x)\right]\\ &- 0.044290\left[\cos(k_x-k_y)+\cos(k_x+k_y)\right] - 0.001678\left[\cos(3k_x)+\cos(3k_y)\right]\\ &- 0.007565\left[\cos(k_x-2k_y)+\cos(2k_x-k_y)+\cos(2k_x+k_y)+\cos(k_x+2k_y)\right]\\ &- 0.001545\left[\cos(k_x-3k_y)+\cos(3k_x+k_y)+\cos(3k_x-k_y)+\cos(k_x+3k_y)\right]\\ &- 0.001888\left[\cos(2k_x-3k_y)+\cos(3k_x+2k_y)\right] - 0.001375\left[\cos(3k_x-3k_y)+\cos(3k_x+3k_y)\right]\\ &- 0.005025\left[\cos(2k_x-2k_y)+\cos(2k_x+2k_y)\right] - 0.001888\left[\cos(3k_x-2k_y)+\cos(2k_x+3k_y)\right] \end{aligned} \tag{S5}$$

$$\begin{aligned}g_{\mathbf{k}} &= 0.007249\left[\cos(k_x-k_y)-\cos(k_x+k_y)\right]\\ &+ 0.001166\left[\cos(k_x-3k_y)-\cos(k_x+3k_y)+\cos(3k_x-k_y)-\cos(3k_x+k_y)\right]\end{aligned} \tag{S6}$$

$$\lambda = 0.028571 \tag{S7}$$

As mentioned in the main text the tight-binding model transforms under the point group $\mathrm{D_{4h}}$. It is invariant under inversions, as well as C_4 rotations with

$$\begin{bmatrix} 0 & 1 & & & & \\ -1 & 0 & & & & \\ & & i & & & \\ & & & 0 & 1 & \\ & & & -1 & 0 & \\ & & & & & -i \end{bmatrix}^{-1} \mathbf{H}_{(-k_y,k_x)} \begin{bmatrix} 0 & 1 & & & & \\ -1 & 0 & & & & \\ & & i & & & \\ & & & 0 & 1 & \\ & & & -1 & 0 & \\ & & & & & -i \end{bmatrix} = \mathbf{H}_{\mathbf{k}} \tag{S8}$$

and σ_v reflections with

$$\begin{bmatrix} 0 & & 1 & & \\ & 0 & & -1 & \\ & & 0 & & 1 \\ 1 & & 0 & & \\ & -1 & & 0 & \\ & & 1 & & 0 \end{bmatrix}^{-1} \mathbf{H}_{(-k_x,k_y)} \begin{bmatrix} 0 & & 1 & & \\ & 0 & & -1 & \\ & & 0 & & 1 \\ 1 & & 0 & & \\ & -1 & & 0 & \\ & & 1 & & 0 \end{bmatrix} = \mathbf{H}_{\mathbf{k}} \tag{S9}$$

and the corresponding rotated σ_v and σ_d mirror planes.

4. Self-Consistent Keldysh Formalism for the Order Parameter Dynamics

a. Model

In the main text, we consider a generic driven multi-band model with attractive interactions and coupled to a fermionic bath. To this end, a generic starting point reads

$$\hat{H} = \hat{H}_{\mathrm{SC}} + \hat{H}_{\mathrm{sub}} \tag{S10}$$

$$\hat{H}_{\mathrm{SC}}(t) = -\sum_{\substack{nm \\ \alpha\beta\sigma}} h^{\alpha\beta}_{n-m}\; e^{-i(\mathbf{r}_{n\alpha}-\mathbf{r}_{m\beta})\cdot\mathbf{A}(t)}\; \hat{c}^{\dagger}_{n\alpha\sigma}\hat{c}_{m\beta\sigma} + \sum_{\substack{nm\alpha\beta \\ \sigma\sigma'}} V^{\alpha\beta}_{n-m}\; \hat{n}_{n\alpha\sigma}\hat{n}_{m\beta\sigma'} - \mu\sum_{n\alpha\sigma}\hat{n}_{n\alpha\sigma} \tag{S11}$$

$$\hat{H}_{\mathrm{sub}} = \sum_{\substack{n\mathbf{k} \\ \alpha\sigma}} \left[g^{\alpha}_{n\mathbf{k}}\; \hat{d}^{\dagger}_{n\mathbf{k}\sigma}\hat{c}_{\mathbf{k}\alpha\sigma} + \mathrm{h.c.} \right] + \sum_{n\mathbf{k}\sigma} \omega_{n\mathbf{k}}\hat{d}^{\dagger}_{n\mathbf{k}\sigma}\hat{d}_{n\mathbf{k}\sigma} \tag{S12}$$

where n, m and α, β denote site and orbital indices, and $h^{\alpha\beta}_{n-m}$, $V^{\alpha\beta}_{n-m}$ parameterize hopping and interaction matrix elements, respectively. Light minimally couples to electrons via Peierls substitution, with $\mathbf{r}_{n\alpha}$ the real-space positions of individual sites and $\mathbf{A}(t)$ the pump field. Furthermore, $g^{\alpha}_{n\mathbf{k}}$ is the tunnel coupling to the substrate, with $\omega_{n\mathbf{k}}$ denoting the substrate dispersion.

The interaction term is taken to be attractive, and is treated in a mean-field approximation for the pairing instability. The corresponding self-consistent dynamics are described by

a generic multi-band BCS model

$$\hat{H} = \sum_{\mathbf{k}} \begin{bmatrix} \boldsymbol{\Psi}^{\dagger}_{\mathbf{k}\uparrow} & \boldsymbol{\Psi}_{-\mathbf{k}\downarrow} \end{bmatrix} \cdot \mathcal{H}_{\mathbf{k}}(t) \cdot \begin{bmatrix} \boldsymbol{\Psi}_{\mathbf{k}\uparrow} \\ \boldsymbol{\Psi}^{\dagger}_{-\mathbf{k}\downarrow} \end{bmatrix} \tag{S13}$$

with the BdG Hamiltonian

$$\mathcal{H}_{\mathbf{k}}(t) = \begin{bmatrix} \mathbf{h}_{\mathbf{k}}(t) & \boldsymbol{\Delta}_{\mathbf{k}}(t) \\ \boldsymbol{\Delta}^{\dagger}_{\mathbf{k}}(t) & -\mathbf{h}^{\star}_{-\mathbf{k}}(t) \end{bmatrix} \tag{S14}$$

where $[\mathbf{h}_{\mathbf{k}}(t)]^{\alpha\beta} = \sum_n h_n^{\alpha\beta}\ e^{-i\mathbf{r}_n\mathbf{k}}$, and

$$\Delta^{\alpha\beta}_{\mathbf{k}} = \frac{1}{L}\sum_{\mathbf{k}'} V^{\alpha\beta}_{\mathbf{k}-\mathbf{k}'} \left\langle \hat{c}_{-\mathbf{k}',\beta\downarrow}\hat{c}_{\mathbf{k}',\alpha\uparrow} \right\rangle \tag{S15}$$

is the multi-band order parameter, subsequently decomposed in terms of the appropriate irreducible representations of the point group as shown in the main text.

b. Equal-Time Keldysh Equations of Motion

Here, we derive the dissipative equal-time equations of motion for superconducting order parameters, for a multi-band BdG superconductor coupled to a fermionic bath. The first step is to derive dissipative equal-time equations of motion. We start from the Keldysh equations of motion in Nambu basis

$$i\partial_t \mathcal{G}_{\mathbf{k}}(t,t') = \mathcal{H}_{\mathbf{k}}(t)\mathcal{G}_{\mathbf{k}}(t,t') + \int d\tau \hat{\Sigma}_{\mathbf{k}}(t,\tau)\mathcal{G}_{\mathbf{k}}(\tau,t') \tag{S16}$$

$$-i\partial_{t'} \mathcal{G}_{\mathbf{k}}(t,t') = \mathcal{G}_{\mathbf{k}}(t,t')\mathcal{H}_{\mathbf{k}}(t') + \int d\tau \mathcal{G}_{\mathbf{k}}(t,\tau)\hat{\Sigma}_{\mathbf{k}}(\tau,t') \tag{S17}$$

where the Keldysh Green's function is written in Larkin-Ovchinnikov form

$$\mathcal{G}_{\mathbf{k}}(t,t') = \begin{bmatrix} \mathcal{G}^R_{\mathbf{k}}(t,t') & \mathcal{G}^K_{\mathbf{k}}(t,t') \\ & \mathcal{G}^A_{\mathbf{k}}(t,t') \end{bmatrix} \tag{S18}$$

The self energy contains the dissipative coupling to the electronic reservoir, and reads explicitly

$$\hat{\Sigma}_{\mathbf{k}}(t,t') = \iint \frac{d\Omega d\omega}{2\pi}\ e^{-i\Omega(t-t')}\left|g_{n\mathbf{k}}\right|^2 \rho_{\mathbf{k}}(\omega)\ \times \\ \times \begin{bmatrix} \frac{1}{\Omega-\omega+i\eta} & -\frac{2i\eta\tanh\left(\frac{\beta\Omega}{2}\right)}{(\Omega-\omega)^2+\eta^2} \\ & \frac{1}{\Omega-\omega-i\eta} \end{bmatrix} \tag{S19}$$

where $\rho_{\mathbf{k}}(\omega)$ is the transverse partial density of states for a 3D bulk/substrate.

In the wide-band limit, $\rho_{\mathbf{k}}(\omega) \to \rho_0$ is taken to be constant. This amounts to a Markov approximation of the retarded component, and the self energy becomes

$$\Sigma_{\mathbf{k}}(t,t') = \int \frac{d\Omega}{2\pi}\, e^{-i\Omega(t-t')} \begin{bmatrix} -i\Gamma & -2i\Gamma \tanh\left(\frac{\beta\Omega}{2}\right) \\ & i\Gamma \end{bmatrix} \tag{S20}$$

$$= \begin{bmatrix} -i\Gamma\ \delta(t-t') & -2\Gamma \left[\beta \sinh\left(\frac{\pi(t-t')}{\beta}\right)\right]^{-1} \\ & i\Gamma\ \delta(t-t') \end{bmatrix} \tag{S21}$$

where $\Gamma = \pi\rho_0|g|^2$ denotes the relaxation constant.

The next task is to derive an equal-time equation of motion for the order parameters. Starting from the Kadanoff-Baym equation, the evolution of the retarded Green's function becomes

$$i\partial_t \mathcal{G}^R_{\mathbf{k}}(t,t') = \mathcal{H}_{\mathbf{k}}(t)\mathcal{G}^R_{\mathbf{k}}(t,t') + \int_{t'}^{t} d\tau\ \Sigma^R(t,\tau)\mathcal{G}^R_{\mathbf{k}}(\tau,t') \tag{S22}$$

$$= \left[\mathcal{H}_{\mathbf{k}}(t) - i\Gamma\right]\mathcal{G}^R_{\mathbf{k}}(t,t') \tag{S23}$$

with $\mathcal{G}^A(t,t') = \left[\mathcal{G}^R(t',t)\right]^\dagger$. The evolution of the Keldysh Green's function reads

$$\partial_t \mathcal{G}^K_{\mathbf{k}}(t,t') = -i\left[\mathcal{H}_{\mathbf{k}}(t) - i\Gamma\right]\mathcal{G}^K_{\mathbf{k}}(t,t') - i\int_{-\infty}^{t'} d\tau\ \Sigma^K(t,\tau)\mathcal{G}^A_{\mathbf{k}}(\tau,t') \tag{S24}$$

$$\partial_{t'} \mathcal{G}^K_{\mathbf{k}}(t,t') = +i\mathcal{G}^K_{\mathbf{k}}(t,t')\left[\mathcal{H}_{\mathbf{k}}(t') + i\Gamma\right] + i\int_{-\infty}^{t} d\tau\ \mathcal{G}^R_{\mathbf{k}}(t,\tau)\Sigma^K(\tau,t') \tag{S25}$$

Define now the equal-time expectation values

$$N^{\alpha\beta}_{\mathbf{k}}(T) = \left\langle \hat{c}^\dagger_{\mathbf{k}\beta}(T)\hat{c}_{\mathbf{k}\alpha}(T)\right\rangle = -\frac{i}{2}\mathcal{G}^K_{\mathbf{k},\alpha\beta}(T,T) + \frac{1}{2} \tag{S26}$$

Its equation of motion can be readily derived as

$$\partial_T N_{\mathbf{k}}(T) = -\frac{i}{2}\left(\partial_t + \partial_{t'}\right)\mathcal{G}^K_{\mathbf{k}}(t,t')\big|_{t=t'=T} \tag{S27}$$

$$= -i\left[\mathcal{H}_{\mathbf{k}}(T),\ N_{\mathbf{k}}(T)\right] - \Gamma\left\{2N_{\mathbf{k}}(T) - 1 - I^K_{\mathbf{k}}(T)\right\} \tag{S28}$$

with

$$I^K_{\mathbf{k}}(T) = \frac{1}{2\Gamma}\int_{-\infty}^{T} d\tau \left[\mathcal{G}^R_{\mathbf{k}}(T,\tau) + \mathcal{G}^R_{\mathbf{k}}(T,\tau)^\dagger\right]\Sigma^K(\tau - T)$$

$$= \frac{1}{2\Gamma}\int_{0}^{\infty} d\tau \left[\mathcal{G}^R_{\mathbf{k}}(T,T-\tau) + \mathcal{G}^R_{\mathbf{k}}(T,T-\tau)^\dagger\right]\Sigma^K(\tau) \tag{S29}$$

with

$$\Sigma^K(t-t') = 2\Gamma\left[\beta\sinh\left(\frac{\pi(t-t')}{\beta}\right)\right]^{-1} \tag{S30}$$

and

$$\begin{aligned}\partial_T\mathcal{G}^R_{\mathbf{k}}(T,T-\tau) = i\mathcal{G}^R_{\mathbf{k}}(T,T-\tau)\left[\mathcal{H}_{\mathbf{k}}(T-\tau)+i\Gamma\right] \\ - i\left[\mathcal{H}_{\mathbf{k}}(T)-i\Gamma\right]\mathcal{G}^R_{\mathbf{k}}(T,T-\tau)\end{aligned} \tag{S31}$$

c. Dissipative BdG Equations of Motion

Now, define the retarded Nambu Green's functions

$$\mathcal{G}^R_{\mathbf{k}}(t,t') = \begin{bmatrix} \mathbf{G}^R_{\mathbf{k}} & \mathbf{D}^R_{\mathbf{k}} \\ -\nu\left(\mathbf{D}^R_{-\mathbf{k}}\right)^\star & -\left(\mathbf{G}^R_{-\mathbf{k}}\right)^\star \end{bmatrix} \tag{S32}$$

where $\nu = +1$ for singlet pairing, $\nu = -1$ for triplet pairing, with normal and anomalous multiband components

$$G^R_{\mathbf{k},\alpha\beta} = -i\theta(t-t')\left\langle\left\{\hat{c}^\dagger_{\mathbf{k}\alpha\sigma}(t),\ \hat{c}_{\mathbf{k}\beta\sigma}(t')\right\}\right\rangle \tag{S33}$$

$$D^R_{\mathbf{k},\alpha\beta} = -i\theta(t-t')\left\langle\left\{\hat{c}^\dagger_{\mathbf{k}\alpha\uparrow}(t),\ \hat{c}^\dagger_{-\mathbf{k}\beta\downarrow}(t')\right\}\right\rangle \tag{S34}$$

Furthermore, define the equal-time function

$$\mathbf{N}_{\mathbf{k}}(t) = \begin{bmatrix} \mathbf{n}_{\mathbf{k}}(t) & \mathbf{f}_{\mathbf{k}}(t) \\ \mathbf{f}^\dagger_{\mathbf{k}}(t) & 1-\mathbf{n}^\star_{-\mathbf{k}}(t) \end{bmatrix} \tag{S35}$$

with expectation values

$$n_{\mathbf{k},\alpha\beta}(t) = \left\langle\hat{c}^\dagger_{\mathbf{k}\beta\sigma}\hat{c}_{\mathbf{k}\alpha\sigma}(t)\right\rangle \tag{S36}$$

$$f_{\mathbf{k},\alpha\beta}(t) = \left\langle\hat{c}^\dagger_{\mathbf{k}\beta\uparrow}\hat{c}^\dagger_{-\mathbf{k}\alpha\downarrow}(t)\right\rangle \tag{S37}$$

Substituting into the equal-time equations of motion derived above, we finally arrive at the closed set of non-linear equations of motion

$$
\begin{aligned}
i\partial_t \mathbf{n}_{\mathbf{k}}(t) &= [\mathbf{h}_{\mathbf{k}}(t),\ \mathbf{n}_{\mathbf{k}}(t)] + \mathbf{\Delta}_{\mathbf{k}}(t)\ \mathbf{f}^{\dagger}_{\mathbf{k}}(t) - \mathbf{f}_{\mathbf{k}}(t)\ \mathbf{\Delta}^{\dagger}_{\mathbf{k}}(t) \\
&\quad - \Gamma\left(2\mathbf{n}_{\mathbf{k}}(t) - 1 - \mathbf{I}^{G}_{\mathbf{k}}(t)\right) \qquad \text{(S38)} \\
i\partial_t \mathbf{f}_{\mathbf{k}}(t) &= \mathbf{h}_{\mathbf{k}}(t)\mathbf{f}_{\mathbf{k}}(t) + \mathbf{f}_{\mathbf{k}}(t)\mathbf{h}_{-\mathbf{k}}(t) \\
&\quad - \mathbf{\Delta}_{k}(t)\left(\mathbf{n}^{\star}_{-\mathbf{k}}(t) - 1\right) - \mathbf{n}_{\mathbf{k}}(t)\mathbf{\Delta}_{k}(t) \\
&\quad - \Gamma\left(2\mathbf{f}_{\mathbf{k}}(t) - \mathbf{I}^{D}_{\mathbf{k}}(t)\right) \qquad \text{(S39)} \\
\mathbf{\Delta}_{k}(t) &= \sum_{\mathbf{k}'} \hat{V}_{\mathbf{k}-\mathbf{k}'}\ \mathbf{f}^{\star}_{\mathbf{k}}(t) \qquad \text{(S40)} \\
\mathbf{I}^{G}_{\mathbf{k}}(t) &= \frac{1}{2\Gamma}\int_0^{\infty} d\tau \left[\mathbf{G}^{R}_{\mathbf{k}}(t, t-\tau) + (\mathbf{G}^{R}_{\mathbf{k}}(t, t-\tau))^{\dagger}\right]\Sigma^{K}(\tau) \qquad \text{(S41)} \\
\mathbf{I}^{D}_{\mathbf{k}}(t) &= \frac{1}{2\Gamma}\int_0^{\infty} d\tau \left[\mathbf{D}^{R}_{\mathbf{k}}(t, t-\tau) + (\mathbf{D}^{R}_{\mathbf{k}}(t, t-\tau))^{\dagger}\right]\Sigma^{K}(\tau) \qquad \text{(S42)} \\
i\partial_t \mathbf{G}^{R}_{\mathbf{k}}(t, t') &= (\mathbf{h}_{\mathbf{k}}(t) - i\Gamma)\,\mathbf{G}^{R}_{\mathbf{k}}(t, t') - \nu\mathbf{\Delta}_{\mathbf{k}}(t)\left(\mathbf{D}^{R}_{\mathbf{k}}(t, t')\right)^{\star} \qquad \text{(S43)} \\
i\partial_t \mathbf{D}^{R}_{\mathbf{k}}(t, t') &= (\mathbf{h}_{\mathbf{k}}(t) - i\Gamma)\,\mathbf{D}^{R}_{\mathbf{k}}(t, t') - \mathbf{\Delta}_{\mathbf{k}}(t)\mathbf{G}^{R}_{\mathbf{k}}(t, t') \qquad \text{(S44)}
\end{aligned}
$$

All simulations presented in the main text follow from numerically integrating the integro-differential equations of motion (S38)-(S44), after decomposing $\hat{V}_{\mathbf{k}}$ and $\mathbf{\Delta}_{\mathbf{k}}$ into the appropriate irreducible representations.

[S1] Eckhart, A. *Rev. Mod. Phys.* **89**, 011004 (2017).

[S2] Kitagawa, T. , Oka, T., Brataas, A., Fu, L. & Demler, E. *Phys. Rev. B* **84**, 235108 (2011).

[S3] Tamai, A. *et al.*, *to be published.*